JOURNAL OF GEOPHYSICAL RESEARCH, VOL. 105, NO. A1, PAGES 361–373, JANUARY 1, 2000

Feasibility of a multisatellite investigation of the Earth's magnetosphere with radio tomography

R. E. Ergun[1], D. E. Larson[1], T. Phan[1], D. Taylor[1], S. Bale[1], C. W. Carlson[1], I. Roth[1], V. Angelopoulos[1], J. Raeder[2], T. Bell[3], U. S. Inan[3], J. -L. Bougeret[4], and R. Manning[4]

Abstract. We describe the scientific motivation, basic principles, and feasibility of a relatively new measurement technique, radio tomography, and show how it can be used to investigate the Earth's magnetosphere. We demonstrate that a multisatellite radio tomography experiment can produce two-dimensional images of plasma density in the Earth's magnetosphere at sufficient spatial (1/2 R_E) and temporal (~10 s) resolution to address key problems of magnetospheric physics. The imaging technique incorporates well-established radio science methods and computed tomography. Several coplanar satellites are required in orbits that encompass the imaged area. We suggest that the large-scale images are more valuable when combined with in situ observations, supporting an unambiguous interpretation of the in situ data and an investigation of the interdependence of small- and large-scale plasma processes.

1. Introduction

Magnetospheric investigations have been gathering valuable in situ observations of magnetospheric plasma, solar wind plasma, and their electromagnetic fields for several decades. These data have been the primary means for studying the complex plasma interactions that occur in critical boundary regions such as the bow shock, the magnetopause [e.g., *Russell*, 1995], the central plasma sheet [*Baker et al.*, 1996, and references therein], and the auroral zone. These data also are the basis of statistical models of the magnetosphere.

There are, however, many open questions on the global nature of magnetospheric processes which cannot be answered with current data. Reconnection, for example, is a key process in solar wind-magnetospheric coupling, yet little is known about its spatial character, its temporal properties, or associated plasma entry [e.g., *Paschmann et al.*, 1979]. The central plasma sheet is the focus of the substorm process, yet little is known about the location, size, and evolution of the dipolarization region nor its relationship with a near-Earth neutral line [*Baker et al.*, 1996]. The cusp region is critical to the origin and fate of magnetospheric plasmas, yet little is known about the relationship between plasma entry and the state of the subsolar reconnection region [*Fuselier et al.*, 1997]. The role of solar wind energy input at the lower-latitude boundary layer is not understood [*Phan et al.*, 1997]. These open questions illustrate the need for multipoint measurements of plasma and electromagnetic fields.

An experimental investigation that provides concurrent measurements of plasma parameters over an extended region of the magnetosphere would have many advantages. Magnetospheric boundaries are in constant motion making single-point observations difficult to interpret. Multipoint observations would resolve the ambiguity of space and time and the interdependence of small-scale plasma phenomena and large-scale magnetospheric processes could be investigated.

There are several approaches that one can use to achieve multipoint observations. In this article, we put forth an approach which combines in situ observations from a moderate number of spacecraft with remote sensing that can make large-scale images of the magnetospheric plasma density. With large-scale imaging, the in situ observations may be analyzed unequivocally. We discuss the scientific motivation, basic principles, and instrumentation of radio tomography, and conclude that radio tomography can produce two-dimensional images of plasma density and density turbulence of the Earth's magnetosphere at sufficient spatial and temporal resolution to address key scientific questions. Radio tomography imaging combines two well-established techniques, radio science and computed tomography. Column density measurements, made by radio wave propagation experiments between two spacecraft, were implemented on the ISEE missions [*Celnikier et al.*, 1983]. Computed tomography has been developed for medical applications [*Lee and Wade*, 1986; *Kak and Slancy*, 1988] and is being used to image plasma density in the ionosphere [e.g., *Fougere*, 1995]. We also show that radio tomography imaging can be made with satellites that can obtain in situ observations.

2. Scientific Motivation

Magnetospheric structures and boundaries are ever changing with solar wind conditions, the interplanetary magnetic field (IMF), and substorm activity. In order to understand and quantify magnetospheric processes, one must understand the electromagnetic field and plasma topology which, in spite of many years of in situ observations, has not been mapped on a global scale. Little is known on the large-scale nature of magnetospheric processes or how small-scale processes couple with each other over large distances. Nor have the current statistical models of the magnetosphere been fully verified.

[1] Space Sciences Laboratory, University of California, Berkeley, CA
[2] Institute of Geophysics and Planetary Physics, University of California, Los Angeles, CA
[3] Stanford Star Laboratory, Stanford University, Stanford, CA
[4] DESPA-URA CNRS 264, Observatoire de Paris-Meudon, France.

Paper number 1999JA900170.
0148-0227/00/1999JA900170$09.00

Global scale observations are therefore one of the natural extensions to the many years of single point, in situ observations.

The scientific value of large-scale images would be greatly enhanced if they are interpreted in conjunction with local plasma and solar wind observations. Activity in the tail strongly depends on the southward component of the IMF as does solar wind plasma entry in the polar cusps [e.g., *Fuselier et al.*, 1991] and low-latitude boundary layer [*Lotko and Sonnerup*, 1995]. Magnetospheric disturbances can be directly driven by changes in the solar wind dynamic pressure.

There is a long list of scientific interests which can be addressed by tomographic imaging. Rather than produce such a list, we choose to concentrate on two regions of interest, the subsolar magnetopause and the near-Earth central plasma sheet. Both regions are at ~8 R_E - 14 R_E.

2.1. Subsolar Magnetopause

The process responsible for transferring the solar wind energy into the magnetosphere begins at the bow shock, ~3 R_E upstream of the Earth's magnetopause. The bow shock is characterized by an increase in plasma density and temperature, a decrease in solar wind velocity, and increased magnetic field turbulence. Upstream of the bow shock are reflected and accelerated electron and ion fluxes which are responsible for exciting a variety of plasma wave modes. The magnetosheath defines the region between the bow shock and magnetopause. It contains the heated and compressed solar wind plasma with density up to 4 times that of the solar wind. Detailed observations show that the bow shock is rarely, if ever, stationary. How the bow shock, magnetosheath, and magnetopause react globally to the passage of interplanetary disturbances such as coronal mass ejections or interplanetary shocks is a subject of current research.

The magnetopause, the boundary between solar plasma and Earth's magnetic field, is also in constant motion, controlled by the solar wind dynamic pressure and IMF. An increased solar wind pressure compresses the magnetopause and moves it earthward while a southward interplanetary magnetic field removes flux from the dayside and adds it to the tail magnetosphere. As the shocked solar wind approaches the magnetopause, the flow deflection and its slowing down around the obstacle results in a possible formation of a shock or standing wave structure. The formation and the evolution of a series of the standing waves requires more quantitative studies [e.g., *Russell*, 1995]. For example, ISEE spacecraft observed numerous examples of a slow mode transition upstream of the magnetopause with large density enhancements. Regions of enhanced and reduced magnetic pressure were interpreted as standing slow-mode structures. The pile-up of magnetic field adjacent to the dayside magnetopause squeezes the plasma out of the region resulting in a low-density region.

The reconnection process is central to understanding solar wind-magnetospheric coupling. Reconnection ultimately determines the size and shape of the magnetic tail and greatly influences energy flow into the tail. Observations at the Earth's magnetopause indicate that magnetic reconnection is time dependent and exhibits significant three-dimensional effects [*Russell and Elphic*, 1979; *Scholer*, 1995]. Several models of the time dependent reconnection include bursty single X-line reconnection [*Scholer*, 1988; *Southwood*, 1988], multiple X-line reconnection [*Lee and Fu*, 1985], and intermittent patchy reconnection [*Russell and Elphic*, 1979]. The three-dimensional topology results in a formation of magnetic flux ropes with multiple reconnection sites, and strong tube-aligned flows are expected as result of the reconnection. The reconnection is also associated with plasma acceleration events in the dayside magnetosphere.

The large-scale structure of the magnetopause needs to be determined to answer questions on reconnection, flux transfer events, and ultimately energy flow and solar wind plasma entry into the magnetosphere. The magnetopause, however, is a very thin boundary and is often difficult to study even with in situ observations due to limited instrument resolution. Fortunately, the state of the magnetopause often influences an extended region upstream in the magnetosheath [*Paschmann*, 1979]. Observations often show high levels of turbulence and plasma wave emissions (e.g., ion cyclotron and whistler waves) in the magnetosheath. A plasma depletion layer is generally observed next to a low-magnetic-shear magnetopause which indicates low transfer levels, while a weak plasma depletion layer under high magnetic shear has been interpreted as evidence for reconnection [*Phan et al.*, 1994]. Comparison of the magnetic field pile up with the plasma density in the magnetosheath can indicate the transfer level across the magnetopause. The best signature of the location of the magnetopause and the state of the magnetopause lies in the plasma density structure and magnetic field structure of the magnetosheath. The plasma flow velocities, turbulence, and the ion and electron temperature are also important parameters that are needed to fully understand the dynamic processes.

2.2. Near-Earth Plasma Sheet

The plasma sheet and its central portion, the current sheet, are the most dynamic regions of the magnetotail. It is there that the currents supporting the antiparallel fields of the magnetotail lobes are confined. It is there that the energy imparted into the magnetosphere from the solar wind, stored in the form of magnetic energy in the Earth's magnetotail, gets transformed into particle energy or currents that influence the auroral ionosphere, the ring current, and the geosynchronous environment. The structure and dynamics of that region currently are studied with single point measurements from one or at most a few spacecraft. Statistical averages of single-point measurements have provided descriptions of a system in which the instantaneous measurements often deviate considerably from the average, thus suggesting that the system is far more complex than the statistical models would suggest.

The extreme variability of the plasma sheet thickness has been known for a long time. During substorm recovery, the plasma sheet can thicken to as much as 8 R_E, whereas during substorm growth phase it can be as thin as 1 R_E or possibly less [*Hones*, 1979; *Pulkkinen et al.*, 1994]. A spacecraft that performs singlepoint measurements cannot remain in the plasma sheet continuously because the plasma sheet oscillates about the GSM XY ($Z = 0$) plane owing to the Earth's rotation. In addition, even if the spacecraft is within the nominal plasma sheet, extreme plasma sheet thinning prior to the onset of geomagnetic activity quite often places the spacecraft outside the active region at the time of onset. Yet it is that parameter, the plasma sheet thickness, which is important to monitor in order to theoretically understand the onset of geomagnetic substorms. With multipoint measurements and global imaging, one can directly determine the plasma sheet thickness at each X distance on the basis of the density profile and from the change in the magnitude of the magnetic field with Z.

The evolution of the above quantities during the course of substorms and convection bay intervals is of primary interest. It is

known that the current sheet thins and moves closer to Earth during substorm growth phase in response to the increased magnetic flux in the magnetotail lobes. The total current sheet thickness and its profile along the X axis are not known, yet they are critical in determining whether current driven instabilities may be responsible for the onset of magnetic substorms [*Coroniti*, 1985; *Lui et al.*, 1991; *Wang et al.*, 1990]. The quantity of interest is the location of maximum current density in relation to the location of onset in space. We need to determine the location of the first change in the magnetic field profile, which is indicative of the onset of magnetic field dipolarization (current disruption [*Lui*, 1991]).

There are a number of questions that can be addressed with global observations of the tail. It is known on the basis of two satellite measurements that magnetic field dipolarization propagates tailward at a rate of ~200 km/s [*Jacquey et al.*, 1993; *Ohtani et al.*, 1992]. What determines the location of the magnetic field dipolarization and how is that related to the history of geomagnetic activity in the tail? How is that related to the ground activity [*Hones*, 1979]? What is the density, and flow profile of the particles that emanate from the magnetic field dipolarization site [*Baumjohann et al.*, 1989; *Hones*, 1979]? Is the earthward flow extended in X, or does it stop just at the edge of the magnetic field dipolarization? Is the tailward velocity of the dipolarization [*Sergeev et al.*, 1995] consistent with flux pile-up at the location of the dipolarization [*Birn and Hesse*, 1991], or is it independent of that, and thus depends on external factors? What is the role of bursty bulk flows? Do they communicate reconnection in the tail to the near-Earth region of the plasma sheet where the dipolarization process begins? Large-scale imaging and multipoint observations can provide time-dependent profiles of density, plasma flow, and magnetic field which can answer some of the above questions.

Snapshots of the plasma sheet at different times would greatly advance our understanding of the behavior of the magnetotail and the substorm process. Ideally, these snapshots would contain high spacial resolution electron and ion distribution functions and electromagnetic fields. Practically, large-scale images will be limited to one or, at best, a few plasma parameters. The above scientific questions and others have motivated the development of an imaging system that can be applied to magnetospheric plasmas.

3. Imaging Technique

The imaging technique that we propose is radio tomography, which uses well-established radio science techniques, wave receiving and transmission instruments, and computed tomography to form high time resolution images of plasma density and density turbulence. It may be possible to measure the magnetic field strength and one component of the plasma velocity with this technique when combined with multipoint, in situ observations. In this article, we concentrate on imaging plasma density.

The basic idea is illustrated in Plate 1 which demonstrates the technique using 16 satellites, 12 of which are in a ~1.1 R_E (geocentric) by 13 R_E polar (90° inclination) orbit and four of which are in a 1.6 R_E by ~8 R_E polar orbit that focus on the subsolar region of the magnetosphere. Plate 2 demonstrates the technique using the same orbits in the magnetotail. The orbits were chosen to optimize both radio tomography imaging and in situ observations and demonstrate that both measurements can be made with the same spacecraft. Plates 1a and 2a display two-dimensional images of the plasma density in the GSM XZ plane (meridianal cut) from a magnetohydrodynamic (MHD) simulation [*Raeder et al.*, 1997]. The color scale represents the plasma density. The two orbits, the instantaneous position of the spacecraft, and the ray paths between the spacecraft are superimposed on the density plot.

Radio tomography imaging works as follows. The spacecraft transmit, in turn, coherently phased pairs of discrete radio frequency signals to be received by all other satellites. The phase difference between the signals yields a very accurate measurement of the integrated electron density along the ray path, generally called "total electron content" (TEC). In Plates 1 and 2, there are 120 lines of sight (the 120 TEC measurements are redundant). The 120 TEC measurements along with 16 local density measurements then can be inverted to produce an image of plasma density in the region encompassed by the satellites. Plates 1b and 2b display reconstructed density images based solely on simulated TEC measurements along the ray paths. The inversion technique is similar to that used in medical computed tomography scans.

The entire tomographic cycle can be as shorts as ~10 s with each satellite transmitting, in turn, every ~0.6 s. Travel times of the signals are less than 0.3 s. The spatial resolution can be as fine as ~1/2 R_E with the orbit configuration in Plates 1 and 2

Designing a radio tomography experiment in the Earth's magnetosphere involves many trade-offs and strongly depends on the region that is investigated. In this article, we concentrate on the magnetosheath and the central plasma sheet at ~8 R_E to ~13 R_E. The analysis and design of an experiment for the ionosphere or plasmasphere would be substantially different from that which we present.

3.1. Radio Science Technique

Radio tomography has been applied to the ionosphere with good success [e.g., *Austen et al.*, 1988; *Raymond*, 1994, *Fremouw et al.*, 1994; *Leitinger*, 1994, *Fougere*, 1995]. Most ionospheric tomography techniques make use of path integrals of electron density. At least five different techniques have been exploited to provide a measure of TEC. These are Faraday rotation, differential phase, group delay, dispersive phase, and elevation angle of arrival [*Davies*, 1990].

Ionospheric radio experiments typically propagate between ground-based systems and spacecraft. The global positioning system (GPS) has also been used to map ionospheric densities. The propagation effects of radio signals transmitted or received from ground-based systems are dominated by the dense F layer of the ionosphere and cannot be used to probe plasmas outside of the ionosphere. Spacecraft-to-spacecraft propagation experiments, however, are ideally suited to study the low-density plasmas in critical regions of the magnetosphere. Radio propagation experiments have been successfully carried out between two spacecraft in the solar wind plasma using the ISEE spacecraft [*Celnikier et al.*, 1983].

For large-scale tomographic imaging of the magnetosphere, the two most straightforward techniques are differential phase [*Leitinger*, 1994] and group delay [*Davies*, 1990]. Usually these two techniques are combined. The differential phase technique requires two phase coherent signals to propagate through the medium. The phase velocity of an electromagnetic wave ($\omega >> \omega_p, \omega_c$) in a plasma is

$$v_\phi \cong c(1 + \omega_p^2/2\omega^2 + \text{ higher order terms}) \quad (1)$$

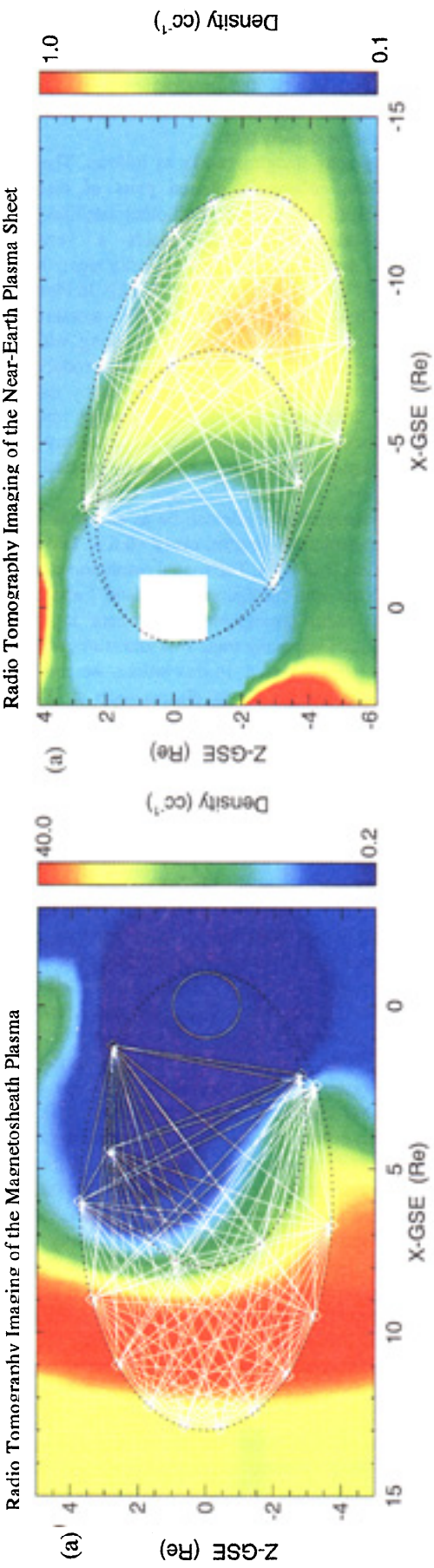

Plate 1. (a) A two-dimensional cut of electron density of the subsolar magnetosheath through the GSM XZ plane based on a three-dimensional MHD model [*Raeder et al.*, 1997]. The orbits, instantaneous positions, and ray paths between 16 satellites are superimposed. (b) The reconstructed density based solely on these 120 simulated total electron count (TEC) measurements. The spacecraft positions are indicated with diamonds.

Plate 2. A demonstration of tomographic imaging in the near-Earth plasma sheet. The display has the same format as Plate 1; the color scales have been adjusted to fit the local plasma densities.

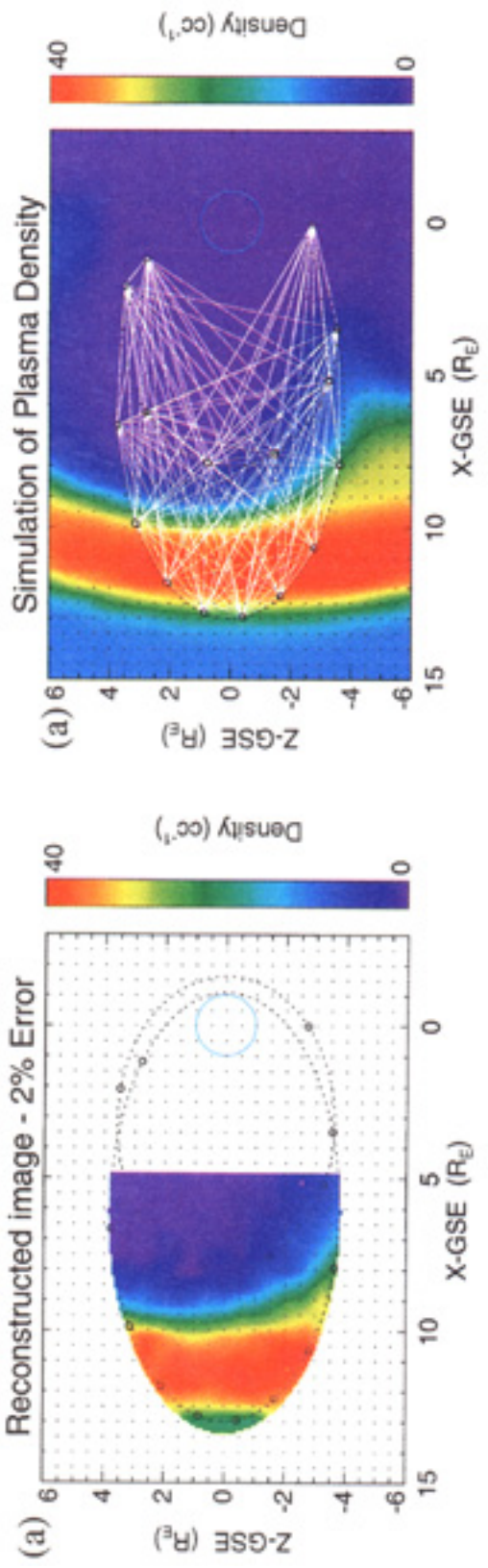

Plate 3. Reconstructed images under 2% and 10% error. Random errors were introduced into the simulated TEC measurements from Plate 1a before creating the images. The image in the top plot (1% error) does not display false features in the magnetosheath and indicates that such errors are acceptable. The bottom plot (10% error) displays features in the magnetosheath where there were none. The bottom image, however, is not completely uncorrelated from that in Plate 1. Even though there are spurious features, the general location, size, and shape of the magnetosheath are retained in spite of the 10% errors. These images demonstrate that the tomographic inversion process is robust under measurement error in the TEC.

Plate 4. (a) The density model from Plate 1 and (b) reconstructed density from the iterative inversion technique. The correlation between the original density and reconstructed density on 1/2 R_E pixels is 0.99

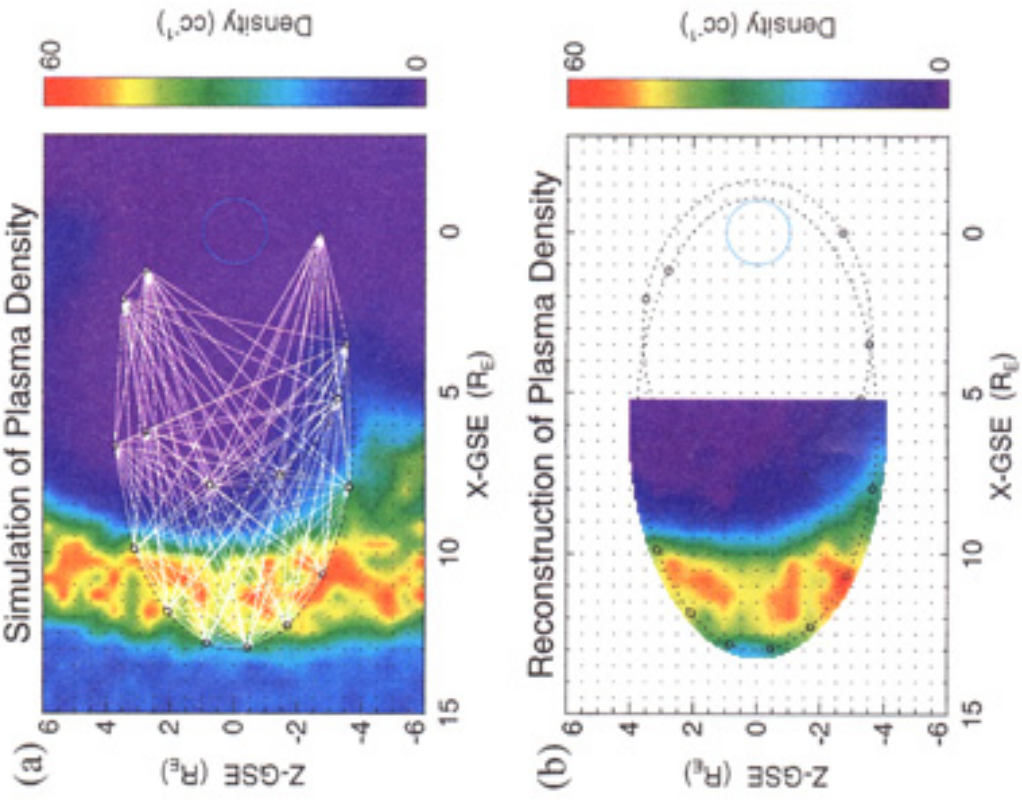

Plate 6. (a) The density model from Plate 1 with a ± 50% random variation on 1/2 R_E pixels. (b) The reconstructed density from the iterative inversion technique. The correlation between the original density and reconstructed density on 1/2 R_E pixels is 0.90.

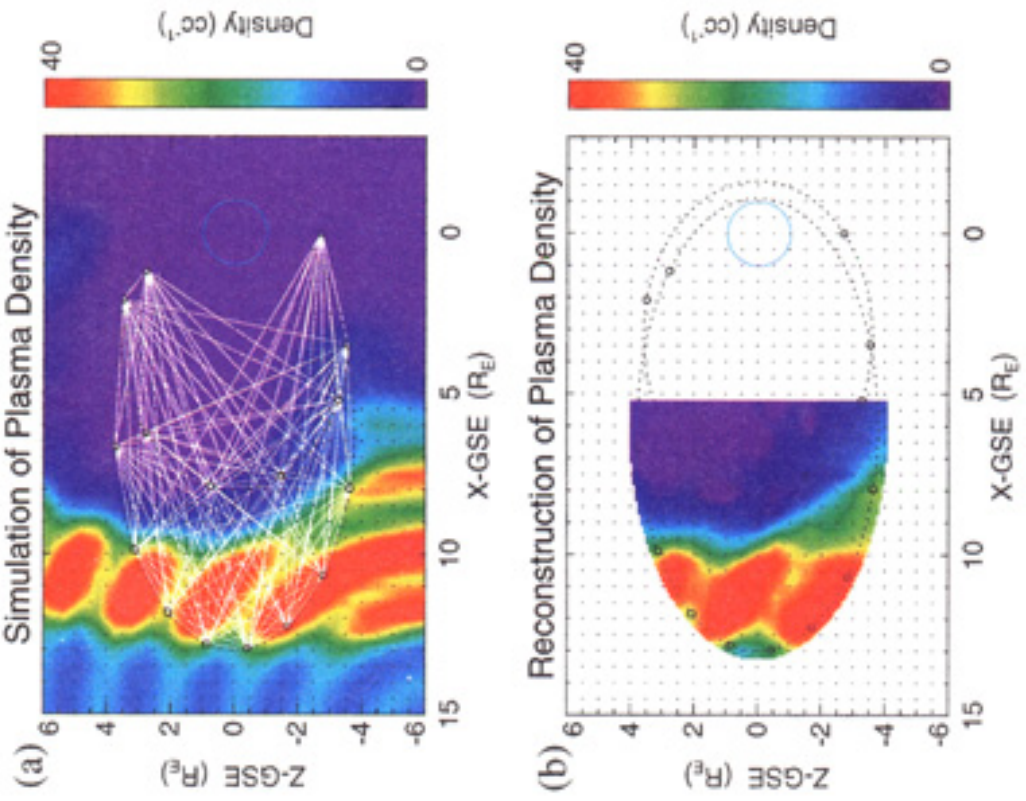

Plate 5. (a) The density model from Plate 1 with a 25% oscillation at 2 R_E wavelength. (b) The reconstructed density from the iterative inversion technique. The correlation between the original density and reconstructed density on1/2 R_E pixels is 0.95.

where ω is the wave frequency, ω_p is the plasma frequency, and c is the speed of light. The higher-order terms depend upon the wave polarization.

The expected phase difference ($\Delta\Phi_1$) between two coherently phased signals with frequencies ω_1 and ω_{ref}, with respect to ω_1 is, to lowest order,

$$\Delta\Phi_1 = \omega_1 \int \left(\frac{1}{v_{\phi ref}} - \frac{1}{v_{\phi 1}} \right) dL \quad (2)$$

Equations (1) and (2) can be combined to get

$$\Delta\Phi_1 \cong \left(\frac{\omega_1 e^2}{2\varepsilon_o m_e c} \right) \left(\frac{1}{\omega_1^2} - \frac{1}{\omega_{ref}^2} \right) \int n dL \quad (3)$$

where e and m_e are electron charge and mass, and n is the plasma density. To first order, the phase difference between the two signals is directly proportional to the TEC ($= \int n dL$) and inversely proportional to the probing frequency (ω_1).

$\Delta\Phi_1$ can be greater than 2π, in which case one needs to resolve the 2π ambiguity. This can be accomplished in a number of ways; the simplest uses the group delay. The delay from the group velocity difference between the two signals is also proportional to the TEC:

$$\Delta t_g \cong -\frac{e^2}{2\varepsilon_o m_e c} \left(\frac{1}{\omega_1^2} - \frac{1}{\omega_{ref}^2} \right) \int n dL \quad (4)$$

The group delay and differential phase measurements can be combined to accurately measure the TEC over a large dynamic range. The group delay of coded signals will yield the coarse value and phase delay the fine value.

In addition to the dc plasma density, a measure of the turbulence level comes from the RMS deviation of $\Delta\Phi_1$. Faraday rotation, proportional to $\pm\omega_c\omega_p^2/\omega^3$ in R and L modes, can be used to determine $\int \boldsymbol{nB} \cdot \boldsymbol{dL}$ in some regions. The Faraday rotation along ray paths through the magnetosheath, for example, should be significant and measurable, reaching >30°, while the Faraday rotation along ray paths through the lobes or central plasma sheet is negligible due to the low plasma density.

3.2. Broadcasting Frequencies

For a given background, a lower-frequency system has a larger differential phase shift ($\Delta\Phi_1$) and, therefore, allows a more accurate determination of the TEC. Lower-frequency signals, however, are more susceptible to disturbances such as refraction and require much longer broadcasting antennae, which may lead to technological limitations. Background is not constant as a function of frequency and therefore is an important factor in choosing the probing frequencies.

Figure 1 displays the expected background at ~10 R_E in the equatorial plane. There are three traces. The dashed line represents the cosmic background noise [*Novaco and Brown*, 1978; *Bougeret*, 1984]. This radiation is ubiquitous and represents the minimum background level that one can expect. The solid line is the average noise measured by the Wind spacecraft [*Bougeret et al.*, 1995] in the range from 8 R_E to 12 R_E during 1996-1998, near solar minimum. The dotted line represents auroral kilometric radiation (AKR) during an intense magnetic substorm at 10 R_E estimated from Fast Auroral Snapshot satellite observations [*Ergun et al.*, 1998].

Wind observations show emissions at a substantially higher level than the cosmic background, particularly at frequencies

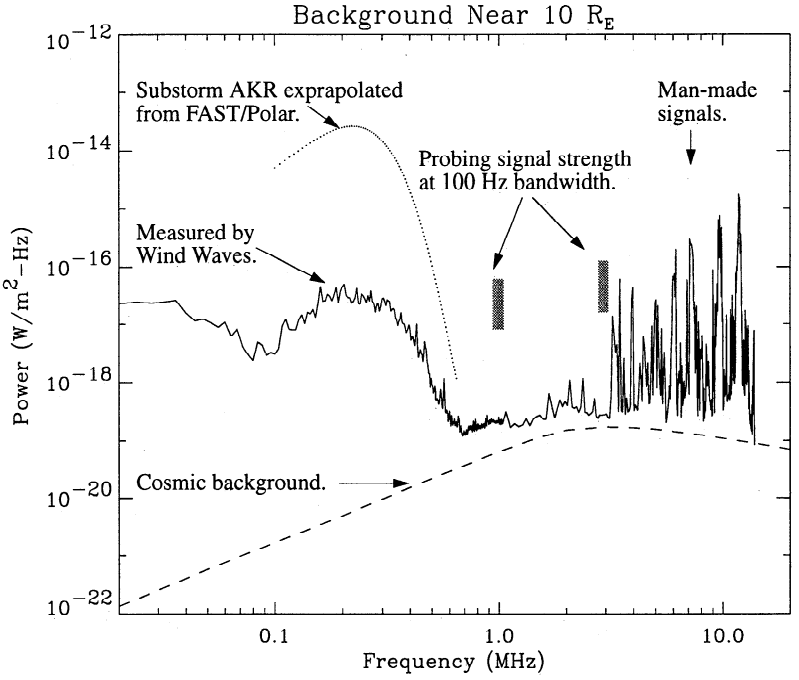

Figure 1. The expected wave electric field background in the near-Earth magnetotail. The solid line represents average spectra from the Wind WAVES instrument between 8 R_E and 12 R_E [*Bougeret et al.*, 1995]. The dashed line is the cosmic background [*Novaco and Brown*, 1978]. The dotted line is the estimated auroral kilometric radiation level during a magnetic substorm based on FAST observations [*Ergun et al.*, 1998]. The rectangles indicate the expected wave power from 2 R_E (top of rectangle) to 12.5 R_E (bottom of rectangles) assuming 20 W radiated power (left rectangle) and 50 W radiated power (right rectangle) and a 100 Hz bandwidth. The signal to noise ratio is ~20 dB and can be improved to ~30 dB by averaging over a 0.1 s period.

greater than ~3 MHz. These emissions are believed to be narrow-band, man-made radio transmissions from Earth. Below ~3 MHz, the ionosphere shields most of the man-made radio signals. This shielding should improve at solar maximum, during which, the ionospheric density increases. Below ~600 kHz, AKR and other naturally generated radio emissions dominate. Intense AKR will be emitted during interesting and perhaps critical states of the magnetosphere, so it is important that a radio science experiment works during the strongest AKR. Inspection of Figure 1 clearly indicates that the ~600 kHz to ~3 MHz band has the lowest background, natural or man-made. There can be other natural emissions that are bursty in nature, such as solar type III radio bursts, that will temporarily increase the background. These emissions, fortunately, are brief and will disrupt << 1% of the measurements.

It may be possible to conduct a radio science experiment with probing frequencies greater than 10 MHz if one uses a band that avoids man-made transmissions. The cosmic background decreases with increasing frequency starting at ~3 MHz. The reduction in background, however, is offset by the smaller phase shift ($\Delta\Phi_1$). The most promising frequency range for radio science probing, considering background and technology, is at ~1 MHz.

3.3. Feasibility

We analyze a system that images regions of the magnetosphere with a probing frequency of 1 MHz (fundamental) and a reference frequency of 3 MHz (third harmonic). The spacecraft depicted in Plates 1 and 2 have a typical separations of ~5×10^7 m (8 R_E). The plasma densities vary from ~0.01 cm^{-3} in the lobes of the magnetotail to ~100 cm^{-3} or more in a compressed magnetosheath. The expected TEC ranges from 5×10^{11} m^{-2} to 5×10^{15} m^{-2}.

A radio science receiver employing the differential phase technique measures the phase difference ($\Delta\Phi_1$) between the two waves. The expected phase delay between two signals with frequencies of 1 and 3 MHz is (from equation (3))

$$\Delta\Phi_1 \cong 8.4\times10^{-13}\int ndL \quad \text{(radians)} \qquad (5)$$

where n (plasma density) is in m^{-3} and L is in m.

We consider the expected signal-to-noise ratio (S/N) to assess the accuracy and feasibility of the TEC measurement. Background noise at ~1 MHz has an intensity of ~1×10^{-19} W/(m^2-Hz) at ~10 R_E the magnetosphere (Figure 1). The probing signals need to be detectable at a distance of ~8 R_E. High background can be overcome with high-powered transmissions, but there are technological limitations to the radiated power from a spacecraft which we discuss below. We consider here, a system which can radiate ~50 W at the third harmonic and ~20 W in the fundamental. The power flux in the fundamental at the receiver, 5×10^7 m away, is ~6×10^{-16} W/m^2. The S/N ratio at the receiver would be ~28 dB (not accounting for losses) when averaged over ~0.1 s. For this S/N ratio, the phase error would be ~2° (arctangent of $(S/N)^{-1}$). Under this error, the minimum TEC that can be detected at 2% accuracy is ~2.5×10^{12} m^{-2} corresponding to an average density along the ray path of 0.05 cm^{-3}.

In principle, the TEC measurement can be made at a precision several times higher than required (see below). In practice, there will be pattern losses (~1 dB) from the transmitter, losses due to orientation of the receiving antennae (~3 dB offset by ~5 dB less cosmic noise due to solid angle coverage of a dipole), and occasionally a higher background. These effects in their most unfavorable state still permits an accurate enough determination of the TEC to image the expected densities in the central plasma sheet, typically ~1 cm^{-3}.

Figure 1 includes two boxes which represent the relative signal strengths at the receiving spacecraft for 20 W radiated in the fundamental and 50 W radiated in the third harmonic. The top of the boxes represents the signal strength under a spacecraft separation of ~2 R_E, the center 5 R_E, and the bottom 12.5 R_E. The signal levels assume a receiver band width of 100 Hz; the S/N ratio can be improved an order of magnitude by averaging over a $\geq$ 0.1 s transmission. Doppler shifts from spacecraft motion can be a high as 50 Hz, but these frequency shifts will not vary significantly during the measuring period so they do not place any restriction on the receiver bandwidth.

Figure 2a displays the expected phase shift ($\Delta\Phi_1$) as a function of average plasma density assuming 1 and 3 MHz probing frequencies at a distance of ~8 R_E. Figure 2b displays the expected error in the TEC averaged over 0.1s. One can see that

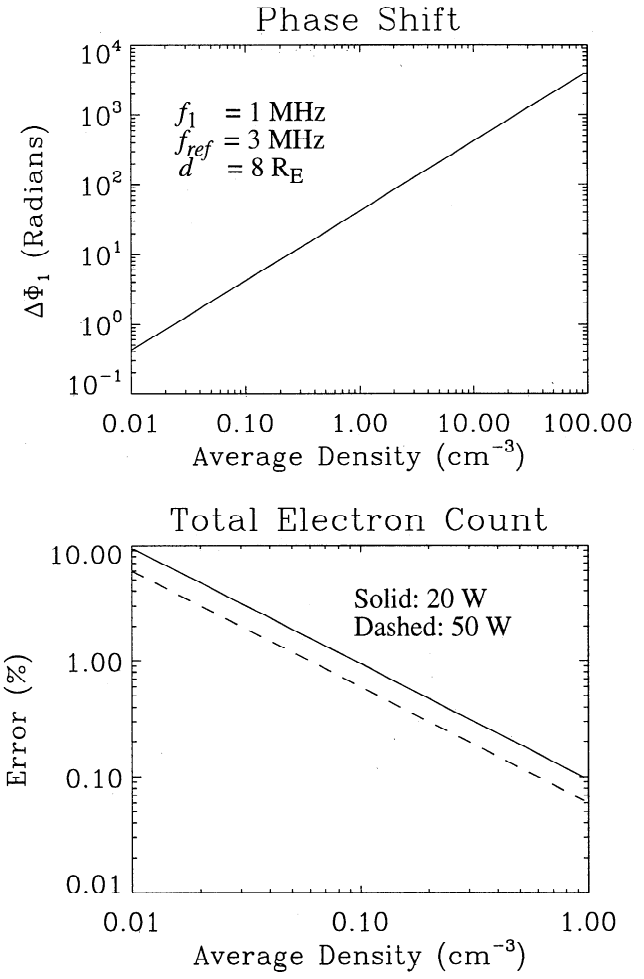

Figure 2. (a) The expected phase shift ($\Delta\Phi_1$) between 1 and 3 MHz probing frequencies over a distance of ~8 R_E (5×10^7 m). (b) The expected error in the total electron content (TEC) measurement as a function of average column density assuming an averaging period of 0.1 s. The error is, to lowest order, independent of spacecraft separation. The top trace is the error under 50 W radiated power, the bottom trace the error under 20 W radiated power. Tomographic inversions require ~2% accuracy in TEC measurements, so a plasma below ~0.05 cm^{-3}, for example, the lobe plasma, cannot be imaged.

~2% errors are achievable for TEC values of ~2.5×10^{12} m^{-2} (average path densities of ~0.05 cm^{-3}). Accuracy can be improved by averaging over longer periods. Interestingly, the accuracy of the determination of the average plasma density along a ray path, to lowest order, does not depend upon the spacecraft separation. For a fixed plasma density, the phase error increases linearly with the separation as does the TEC.

There are several other possible sources of error. Appendix A discusses ray refraction from density gradients. Refraction is negligible for most magnetospheric applications, but can be appreciable if the density variations are large, for example in a compressed magnetosheath, limiting the maximum density that can be probed (1 MHz signal at ~2% accuracy) to ~100 cm^{-3}. Appendix B discusses reflections from the ionosphere which can affect near-Earth spacecraft.

3.4. Tomographic Image Construction

Tomographic techniques have been used in medical science for decades [*Lee and Wade*, 1985; *Kak and Slancy*, 1988]. Although tomographic imaging is commonly believed to be a new field, the mathematical foundation was discussed by Radon as early as 1917 [*Deans*, 1983]. In its simplest form, the magnetospheric tomography problem can be posed as follows: given a localized region and the TEC between all spacecraft pairs, can a unique image of the plasma density be constructed? There is a broad class of images for which a unique solution does exist, as demonstrated through the back projection theorem [*Bracewell*, 1956]. Many techniques exist to perform the tomographic inversion [e.g., *Fougere*, 1995].

Tomographic inversion processes for radio propagation experiments differs somewhat from those used in medical science. In medical imaging, the relation between fluxes of penetrating X-rays and the column density along the ray path is logarithmic. This relation limits the dynamic range of medical scans but allows for detection of small variations of density about a norm. The measured phase shift ($\Delta\Phi_1$) in a radio propagation experiment is directly proportional to the TEC. Thus radio tomography does not suffer from a limited dynamic range and is well-suited for investigating the magnetosphere. Furthermore, $\Delta\Phi_1$, a phase shift, can be very accurately measured as demonstrated above, so small variations also can be detected. On the other hand, medical scans typically have $>10^4$ column densities (or pixels) resulting in very fine-scale images. Magnetospheric radio tomography experiments are limited to $N_{sc}*(N_{sc}-1)/2$ pixels, where N_{sc} is the number of spacecraft. Under current technology, the images have 100 to 500 pixels. An inversion algorithm for radio science must properly transform underdetermined, unevenly distributed TEC measurements into images.

3.5. Least Squares Inversion

We discuss two types of inversion methods which can be applied to magnetospheric imaging. The method used to reconstruct the images shown in Plates 1 and 2 employed inherently smooth, two-dimensional functions to represent the density:

$$\ln[n(x,y)] = \sum_{i=0}^{N-1} C_i D_i(x,y) \ln[D_i(x,y)] + C_N + C_{N+1}x + C_{N+2}y \quad (6)$$

where

$$D_i(x,y) = sqrt[(x - X_i)^2 + (y - Y_i)^2] \quad (7)$$

Here n is the plasma density and X_i and Y_i are the location of function i in the image (x,y) plane. Using least squares analysis, the parameters C_i are calculated such that the computed column densities match the measured values. This method, initially developed to reconstruct two-dimensional distribution functions, has the advantage of allowing the image resolution to be controlled. The sets, X_i and Y_i can be adjusted to have better resolution in those portions of the image that are warranted. The algorithm can be easily adopted to include the measured density at each of the spacecraft to enhance the image. Previous and following images can also be weighted into the least square fit to increase resolution or accuracy.

The images in Plate 1 were constructed using TEC values that were exact while the measured values of TEC are expected to have errors. The effects of observational errors on the reconstructed images are very difficult to depict mathematically, so we use an empirical approach. Plate 3 displays reconstructed images with random errors of 2% (Plate 3a) and 10% (Plate 3b). The reconstructed image of Plate 3a (2% error) differs very little from Plate 1, except in the regions near Earth where the point density is sparse. As demonstrated by this example, empirical tests indicate that 2% error in the TEC measurement is acceptable. The reconstructed image in Plate 3b, however, is unacceptable to the authors. The image indicates structure in the magnetosheath where there was none. The image in Plate 3b, however, remains correlated with that in Plate 1. Even though there are spurious features, the general location, size, and shape of the magnetosheath is retained in spite of the large errors. These data demonstrate how the tomographic inversion process is robust under measurement error.

Another possible source of error can come from sample aliasing. Density variations with wavelengths far less than the pixel size produce little error while variations larger that the pixel size are properly imaged. Density variations, however, that have wavelengths of approximately the pixel spacing, or temporal variations approximately the sample time, may cause errors in the reproduced image. The image that results from tomographic inversion may not be unique but depends upon the inversion method. Fortunately, scintillations can be used to test for the presence of small-scale structure (see Appendix C). The least squares technique above results in a overly smooth image which does not appear to generate false fine-scale structure but, on the other hand, can hide actual fine structure.

3.6. Iterative Reconstruction

The second inversion method that we discuss uses an algorithm modeled after the volumetric simultaneous iterative reconstruction technique [*Bernhardt et al.*, 1998, and references therein]. The algorithm, designed to reconstruct underdetermined images, starts with evenly spaced pixels, whose number can exceed the number of ray paths. The TEC on the reconstructed pixel map is approximated by summing the contributions that the ray path makes through each of the pixels (its length through the square pixel) times the density assigned to the pixel [see *Bernhardt et al.*, 1998, Figure 3]. The iterative process has two steps. The difference between the actual TEC and that in the reconstructed pixel map is distributed along the ray path in proportion the distance the ray path has in each pixel. The density is then allowed to "diffuse" to the nearest neighbors. The diffusion is mathematically performed by convolving a mask over the entire area. The diffusion step is followed by another TEC correction step, and so on.

The amount of density "diffusion" is controlled by a parameter called the "temperature." With a lower temperature, less density can diffuse into the nearest neighbors during an iteration. As the iterative cycle continues, the temperature is slowly lowered. The solution converges to the a pixel representation of the density that satisfies the TEC measurements and has the least variation between nearest neighbors, in other words, the smoothest solution.

The underdetermined reconstruction results in a "defocused" image of the actual density. If the actual density is smooth, the reconstructed image is near perfect. Plates 4a and 4b display an example reconstruction of a smooth density image. In this example, the correlation between the initial density map and the reconstructed image is 0.99. Plates 5a and 5b display a reconstruction of a moderately irregular density image. A wave was artificially forced on the MHD simulation results (25% amplitude with a 2 R_E wavelength). The algorithm reproduces the features well but somewhat smooths out the wave. The correlation between the initial density and the reconstructed image is 0.95. Plates 6a and 6b have a highly irregular initial density. The MHD simulation results (Plate 4) were randomly varied on 1/2 R_E pixels by as much as $\pm$ 50%. The reconstructed image appears to be smoothed but maintains the general appearance of the initial map. The largest deviation comes at Y= -0.5, X=11.5; a strong density enhancement is only barely visible in the reconstruction. The correlation between the initial density and the reconstructed image is 0.90.

The inverted images have the highest spatial resolution where the ray paths are concentrated. The above orbits concentrate the ray paths in the magneosheath, so that area is reproduced with the best spatial resolution and accuracy. Areas with low ray path concentrations were not as well reconstructed. The iterative reconstruction algorithm has similar error tolerance as the least squares algorithm. Thus we have demonstrated that at least two distinct reconstruction algorithms can properly reconstruct tomographic images of magnetospheric plasma to ~1/2 R_E resolution.

4. Radio Tomography Instrument

A radio tomography experiment in the Earth's magnetosphere requires multiple satellites, each of which are capable of transmitting and receiving radio signals. These satellites must typically encompass the region to be imaged but can be situated inside the image plane. In situ observations are of great importance, so one must design the experiment to satisfy both in situ observations and tomographic imaging requirements. We briefly discuss orbits and features of transmitters and receivers that are needed to satisfy the experimental requirements.

4.1. Orbits

The satellites must be placed in orbits such that density images can be reconstructed uniquely. There are three clear requirements. The spacecraft must be coplanar and the TEC measurements must have a representative sample of all directions through the image plane. The orbit design also should concentrate the ray paths in the most critical areas. These requirements are met for the two regions specified in this article with spacecraft placed in at least two different orbits. In Plates 1 and 2 the spacecraft are phased in two highly eccentric orbits. The outer orbit is 1.1 R_E (geocentric) by 13 R_E orbit and the inner orbit is 1.6 R_E by 8 R_E. Both orbits are at 90^o inclination. These orbits were designed so that the right ascensions of the ascending nodes and the arguments of perigee remain the same. Thus the spacecraft will maintain the relative configuration depicted in Plates 1 and 2. Typically, it is not possible to obtain a sufficient angular sampling with spacecraft phased in only one orbit as the Earth will block rays along the major axis.

Empirical tests indicate that precise positioning of the spacecraft on the image plane is not necessary. For the magnetospheric conditions of Plates 1 and 2, for example, the spacing between the spacecraft can vary by as much as 50% without noticeable degradation of the image reconstruction. Errors that arise from one or more of the spacecraft lying out of the image plane cannot be easily quantified. These errors would depend upon the density gradients normal to the image plane.

4.2. Radio Tomography Transmitter

We consider an instrument which uses 1 and 3 MHz frequency probing frequencies. For these wavelengths (λ, 100 m and 300 m), the natural choice of spacecraft antenna is a half-wave dipole. To maximize the radiated power, the antennae elements should be 1/4 λ in length (1/2 λ tip-to-tip). Such tuned dipole antennae can be very efficient and are not expected to suffer significant reflection loss or pattern loss if the spacecraft body is comparatively small. The same antennae can be used both to transmit and receive.

Radio tomography requires two distinct-frequency carriers, and it is not practical to tune both signals. The system needs to be designed for maximum efficiency at the third harmonic since more power is required (Figure 1). A 25 m (50 m tip-to-tip) antenna system is tuned for 3 MHz with a relative band width of ~2%. The ohmic resistance of the antenna (e.g., 26 gauge Be-Cu wire) can be less than the radiation resistance (~78 Ω), which would allow for >50% antenna efficiency. The fundamental would be untuned and would have far less radiated power if driven with the same voltage as the third harmonic [*Calvert, et al.*, 1995]. By driving a square wave at the fundamental frequency (1 MHz) (which has 1/3 the drive Voltage at the third harmonic) and externally tuning the antennae the fundamental can be somewhat enhanced. With optimal matching of transmitter circuitry which can be achieved with discrete frequency systems, power converter and other losses are such that one can achieve >30% total efficiency. Such a transmitting system would yield ~20 W of radiated power at the fundamental and ~50 W of radiated power at the third harmonic from a 250 W transmitter. This power level needs to be sustained >0.1 s every ~10 s, requiring an average of >2.5 W of power.

The transmitter requirements are well within known instrument capabilities. Wire booms of greater than 50 m tip-to-tip have been successfully deployed on several missions (most recently FAST [*Ergun, et al.*, The FAST satellite electric and magnetic field instrument, submitted, *Space Sci. Rev.*, 1998.]) and 2.5 W of average power is well within a small spacecraft resource. The constant surging of 250 W, however, may present a large stress on the power system. A 0.1 s surge at 250 W (25 J) could be sustained by capacitors of > 0.1 F at ~30 V. Such large capacitances have recently become available.

4.3. Radio Tomography Receiver

The radio tomography receiver must measure phase and group delays between two phase coherent signals and their relative polarization. The phase differences between a 1 and 3 MHz signals (equation (4)) range from ~0.75 radians (~43^o) in the lobe

region to ~7500 radians (~1200 x 360°) in a compressed magnetosheath. Differential group delays are expected to be from 0.12 μs to 1.2 ms. There are a number of signal processing techniques that have been developed for radio science which can be used in this experiment. A receiver for the described experiment would require a combination of relative group delay and phase difference measurements. The group delay would yield a coarse estimate of the TEC and the phase shift a more exact value. The expected errors in the phase delay (~2°) and group delay (~1 μs) allow an accurate enough determination of the TEC for tomographic inversion.

Receiving radio frequency signals in space with wire antennae is well established and, once again, has been accomplished in many previous experiments. Typical preamplifier noise levels ($1x10^{-17}$ V^2/Hz) and thermal noise levels (~$1x10^{-18}$ V^2/Hz at 1 MHz with 1 μA of photoemission current) are far lower than the background or signal strength and should not require any special design considerations for a radio tomography mission.

5. Conclusions

For many years, in situ observations of plasma and electromagnetic fields from single spacecraft have provided the basis for investigating the magnetosphere. Many of the remaining problems, however, require concurrent, multipoint observations so that the data can be unambiguously interpreted as spatial or temporal phenomena, and the interdependence of small-scale plasma phenomena and large-scale magnetospheric processes can be investigated. We suggest an approach that combines large-scale imaging with in situ observations.

We demonstrated that radio tomography imaging can provide large-scale images of plasma density with sufficient resolution (~1/2 R_E, ~10 s) to address key scientific questions of magnetospheric physics. We have, one at a time, discussed the issues of transmission and receiving, background noise, underdetermined images, measurement errors, ray refraction, ionospheric reflection, grazing incidence, and density turbulence (scintillations). These ultimately need to be combined into a single algorithm. There exist robust tomographic algorithms that are tolerant of error. Empirical tests indicate that tomographic inversions require TEC observations with less than ~2% error. The frequency band between ~600 kHz and ~3 MHz provides an excellent domain of low-noise background. A satellite-borne radio science experiment can measure the TEC with the needed accuracy to image the plasma sheet and magnetosheath. The needed experimental apparatus, wire booms, transmitters, and receivers are available under current technologies. A radio propagation experiment has been flown before on the ISEE spacecraft.

One of the challenges is to deploy 10 to 20 satellites into the appropriate orbits. Such operations have been done for the communications industry and, with the development of small-mass satellites, a radio tomography experiment can be carried out with a single launch vehicle. We have been able to describe orbits in which both in situ observations and radio tomography imaging can be performed by the same spacecraft. The combination of global imaging and multipoint, in situ observations can uniquely advance our understanding of the magnetosphere.

Appendix A: Ray Refraction

Error in the TEC measurement can result from ray refraction. The refracted ray path not only samples neighboring plasma rather than the plasma directly between two spacecraft but also travels a longer distance. It is the latter effect that can introduce the most sizable error.

Ray refraction can be estimated in two ways. One may assume the density gradient is normal to the ray path over an extended distance. In other words, the ray grazes a density boundary. With grazing incidence, a ray can experience strong refraction, but with low probability. To understand refraction from grazing incidence, one must estimate the density gradient and the distance that the ray will experience this gradient, both of which are difficult to quantify. In the more typical case, the ray refracts at a boundary that it approaches obliquely. We discuss both approaches below.

A1. Ray Refraction at an Oblique Boundary

In the geometry depicted in Figure 3, the probing ray, transmitted from spacecraft SC1, follows ray path A, refracting at a sharp density boundary before being received by SC2. The reference ray follows ray path B, a straight line between SC1 and SC2. The difference between the two path lengths depends on the refraction angle δθ. This angle can be estimated by using Snell's law. For simplicity, we assume that one side of the density boundary is a vacuum. On the other side, we use the ordinary mode dispersion, neglecting a magnetic field:

$$\omega^2 = \omega_p^2 + c^2 k^2 \tag{8}$$

Under Snell's law, assuming small angle refraction, ray refraction (δθ) can be estimated as

$$\delta\theta \cong \frac{\omega_p^2}{2\omega^2}\frac{k_{\|}}{k_{\perp}} \tag{9}$$

where $k_{\|}$ ($k_{\perp}$) is the component of the wave vector parallel (perpendicular) to the density boundary. The difference in path length can be estimated as

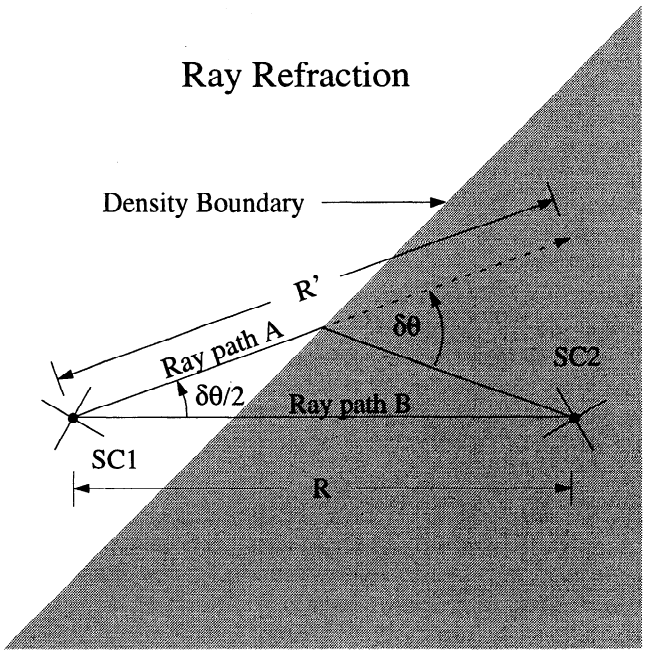

Figure 3. A diagram depicting ray refraction at an oblique boundary. The increased path length can cause an error in the TEC measurement.

$$\Delta R = R' - R \cong \frac{R}{32}\frac{\omega_p^4 k_\parallel^2}{\omega^4 k_\perp^2} \quad (10)$$

In this example, the error due to ray refraction ($\Delta\Phi_R/\Delta\Phi_1$) is the ratio of the increase in phase shift from the longer path length ($\Delta\Phi_R = k\Delta R$) to the expected phase shift (equation (3), assume that one half of the path is in the region of high plasma density, $\omega = \omega_1$, and that $\omega_{ref} >> \omega_1$):

$$\frac{\Delta\Phi_R}{\Delta\Phi_1} \cong \frac{\omega_p^2}{8\omega^2}\frac{k_\parallel^2}{k_\perp^2} \quad (11)$$

From (11), it is clear that ray refraction can be neglected for most magnetospheric applications since $\omega >> \omega_p$. For example, the typical plasma density of the magnetosheath is ~20 cm^{-3}. With a 1 MHz probing frequency and a grazing angle such that $k_\parallel / k_\perp = 1$ to 10, the refractive error is ~0.02% to ~2%. However, a severely compressed magnetopause could have a plasma density as high as 100 cm^{-3}. With a grazing angle such that $k_\parallel / k_\perp = 10$, the refractive error can exceed 10%. Ray paths that penetrate a highly compressed magnetosheath or the plasmasphere, even for short distances, could suffer strong refraction with a 1 MHz probing frequency.

A2. Grazing Incidence

Refraction from an abrupt density gradient nearly normal to the ray path ($k_\parallel >> k_\perp$) is

$$\delta\theta \cong \omega_p/\omega \quad (12)$$

Refraction of a grazing ray can be much more severe ($\Delta\Phi_R/\Delta\Phi_1 \cong 1$) than that of an oblique ray. Significant refraction from grazing incidence, however, requires a remarkably unfortunate situation whereby the wave follows an abrupt density boundary for a distance (D) many times the perpendicular scale length of the density gradient ($\Delta D_\perp \cong [d\ln(n)/dr_\perp]^{-1}$, where $r_\perp$ is perpendicular to the ray path). This condition is roughly expressed as: $\Delta D_\perp \cong D\sin(\delta\theta)$. which, when combined with equation (12), indicates a ray path that follows a 100% gradient ($\Delta D_\perp \cong 250$ km, a typical proton gyroradius) for ~1 R_E. In practice, the probability of such an occurrence is very low.

Finally, even though errors due to grazing incidence can be large, they have only a small effect on tomographic image construction. The effect is such to shift the position of density boundary along the direction of the gradient. Once the tomographic image is constructed, one can iterate the inversion to correct for ray refraction to first order. Furthermore, magnetospheric boundaries are in constant motion as are the spacecraft, so such an unfortunate ray path should appear in one or at most a few images. We conclude than radio tomography can be used to image densities up to ~100 cm^{-3}.

Appendix B: Ionospheric Reflections

We examined the possibility of interference from ionospheric reflections. For spacecraft more than ~2 R_E from Earth, in the worst-case scenario (perfect reflection), strength of the reflected signals can be expressed as the small target radar equation [*Calvert et al.*, 1995]:

$$\Psi_r \cong \frac{R_E^2 P_o}{16\pi s^4} \quad (13)$$

where P_o is the radiated power from one spacecraft, and s is the mean distance from Earth to the transmitting and receiving spacecraft. The power flux of the reflected signal will be less than 1% of the primary signal if the mean distance of the from Earth is more than 5 R_E, given that the spacecraft separation is ~s. Of the 120 ray paths in Plates 1 and 2, only two (the vertical paths near Earth) could experience interference from ionospheric reflections. Those ray paths could be removed from the image reconstruction if necessary.

Appendix C: Scintillations

The radio tomography experiment as designed is sensitive to structures as small as ~1/2 R_E, but would not necessarily properly reconstruct smaller structures, so it is important to determine if, and to what degree, small-scale structures may reduce the accuracy of the inversion. One such metric which can be used is scintillation.

Scintillation or amplitude modulation comes from refracted rays that interfere with the primary ray. The most effective amplitude modulations come if the refracted ray path is 1/2 λ longer than the primary ray path, where λ is the wavelength. Such refraction can be produced by a structure that has a scale size normal to the ray path (or Fresnel size) of $S \cong \sqrt{\lambda D}$, where D is the distance between the spacecraft. Since $D \cong 5x10^7$ m and λ = 300 m, the Fresnel size is ~1.2 x 10^5 m (~120 km), which is very close to the expected proton gyroradius in the magnetosheath and plasma sheet (250 km with B = 10 nT and T_i = 500 eV). Amplitude modulations that arise from interference from refracted ray paths would therefore reflect turbulence on ion-gyroradius scale sizes. Strong scintillation would indicate small-scale (<1/2 R_E) turbulence and thus can be used as a measure of the accuracy of the tomographic inversion.

Acknowledgments. The authors thank engineers Henry Primbsch and Dave Pankow for their valuable advise. This work was supported by NASA's New Missions Concept Program, NAG-53916.

Hiroshi Matsumoto thanks T. Aso and B. W. Reinisch for their assistance in evaluating this paper.

References

Austen, J. R., S. J. Franke, and C. H. Liu, Ionospheric Imaging using computerized tomography, *Radio Sci., 23*, 299, 1988.

Baker, D. N., T. I. Pulkkinen, V. Angelopoulos, W. Baumjohann, and R. L. McPherron, Neutral line model of substorms: Past and present views, *J. Geophys. Res., 101*, 12975, 1996.

Baumjohann, W., G. G. Paschmann, and C. A. Cattell, Average plasma properties in the central plasma sheet, *J. Geophys. Res., 94*, 6597, 1989.

Bernhardt, P. A., et al., Two-dimensional mapping of the plasma density in the upper atmosphere with computerized ionospheric tomography, *Phys. Plasmas, 5*, 2010, 1998.

Birn, J., and M. Hesse, The substorm current wedge and field-aligned currents in MHD simulations of magnetotail reconnection, *J. Geophys. Res., 96*, 1611, 1991.

Bougeret, J. -L., J. Fainberg, and R. G. Stone, Interplanetary radio storms, I, Extension of solar active regions through the interplanetary medium, *Astron. Astrophys., 136*, 255, 1984.

Bougeret, J. -L., et al., WAVES: The radio and plasma wave investigation on the Wind spacecraft, *Space Sci. Rev., 71*, 231, 1995.

Bracewell, R. N., Strip integration in radio astronomy, *Aust. J. Phys., 9*, 198, 1956.

Calvert, W., R. F. Benson, D. L. Carpenter, S. F. Fung, D. Gallagher, J. L. Green, P. H. Reiff, B. W. Reinisch, M. Smith, and W. W. L. Taylor, The feasibility of radio sounding of the magnetosphere, *Radio Sci., 30*, 1577, 1995.

Celnikier, L.M., C. C. Harvey, R. Jegou, M. Kemp, and P. Moricet, A

determination of the electron density fluctuation spectrum in the solar wind using the ISEE propagation experiment, *Astron. Astrophys., 126*, 293, 1983.

Coroniti, F. V., The growth and expansion phases of magnetospheric substorms, *J. Geophys. Res., 90*, 7427, 1985.

Davies, K., *Ionospheric Radio*, *IEEE Electromagn. Waves Ser.*, vol. 31. Peregrinus, London, 1990.

Deans, S.R., *The Radon Transform and Some Applications*, John Wiley, New York, 1983.

Ergun, R. E., et al., FAST satellite wave observations in the AKR Source region, *Geophys. Res. Lett., 25*, 2061, 1998.

Fougere, P. F., Ionospheric radio tomography using maximum entropy, *Radio Sci., 30*, 429, 1995.

Fremouw, E. J., J. A. Sccan, R. M. Bussey, and B. M. Howe, A status report on applying discrete inverse theory to ionospheric tomography, *Imag. Sys. Technol., 5*, 97, 1994.

Fuselier, S. A., D. M. Klumpar, and E. G. Shelley, Ion reflection and transmission during reconnection at the Earth's subsolar magnetopause, *Geophys. Res. Lett., 18*, 139, 1991.

Fuselier, et al., Bifurcated cusp ion signatures: Evidence for re-reconnection? *Geophys. Res. Lett., 24*, 1471, 1997.

Hones, E. W., Jr., Transient phenomena in the magnetotail and their relation to substorms, *Space Sci. Rev., 23*, 393, 1979.

Jacquey, C., J. A. Sauvaud, J. Dandouras, and A. Korth, Tailward propagating cross-tail current disruption and dynamics of near-Earth tail: A multipoint measurement analysis, *Geophys. Res. Lett., 20*, 983, 1993.

Kak, A. C., and M. Slaney, *Principles of Computerized Tomographic Imaging*, IEEE Press, New York, 1988.

Lee, H., and G. Wade, *Imaging Technology*, IEEE Press, New York, 1986.

Lee, L. C., and Z. F. Fu, A theory of magnetic flux transfer at the Earth's magnetopause, *Geophys. Res. Lett., 12*, 105, 1985.

Leitinger, R., Data from orbiting navigation satellites for tomographic reconstruction, *Imag. Sys. Technol., 5*, 85, 1994

Lui, A. T. Y., A synthesis of magnetospheric substorm models, *J. Geophys. Res., 96*, 1849, 1991.

Lui, A. T. Y., C.-L. Chang, A. Mankofsky, H.-K. Wong, and D. Winske, A cross-field current instability for substorm expansions, *J. Geophys. Res., 96*, 11389, 1991.

Lotko, W., and B. U. O. Sonnerup, The low-latitude boundary layer on closed field lines, in *Physics of the Magnetopause*, *Geophys. Monogr. Ser.*, vol. 90, edited by P. Song, B. U. O. Sonnerup, and M. F. Thomsen, p. 371. AGU, Washington, D. C., 1995.

Novaco, J.C., and L.W. Brown, Nonthermal galactic emission below 10 megahertz. *Astrophys. J., 221*, 114, 1978.

Ohtani, S., S. Kokubun, and C. T. Russell, Radial expansion of the tail current disruption during substorms: A new approach to the substorm onset region, *J. Geophys. Res., 97*, 3129, 1992.

Paschmann, G., B. U. O. Sonnerup, I. Papamastorakis, N. Sckopke, G. Haerendel, S. J. Bame, J. R. Asbridge, J. T. Gosling, C. T. Russell, and R. C. Elphic, Plasma acceleration at the Earth's magnetopause: Evidence for reconnection, *Nature, 282*, 243, 1979.

Phan, T. -D., G. Paschmann, W. Baumjohann, N. Sckopke, and H. Luhr, The magnetosheath region adjacent to the dayside magnetopause: AMPTE/IRM observations, *J. Geophys. Res., 99*, 121, 1994.

Phan, T. -D., D. Larson, J. McFadden, C. Carlson, M. Moyer, K.I. Paularena, M. McCarthy, G.K. Parks, H. Reme, T.R. Sanderson, and R.F. Lepping, Low-latitude dusk flank magnetosheath, magnetopause, and boundary layer for low magnetic shear: Wind observations, *J. Geophys. Res., 102*, 19883, 1997.

Pulkkinen, T. I., D. N. Baker, D. G. Mitchell, R. L. McPherron, C. Y. Huang, and L. A. Frank, Thin current sheets in the magnetotail during substorms: CDAW 6 revisited, *J. Geophys. Res., 99*, 5793, 1994.

Raeder, J., J. Berchem, M. Ashour-Abdalla, L. A. Frank, W. R. Paterson, K. L. Ackerson, R. P. Lepping, S. Kokubun, T. Yamamoto, and S. A. Slavin, Boundary layer formation in the magnetotail: Geotail observations and comparisons with a global MHD model, *Geophys. Res. Lett., 24*, 951, 1997.

Raymond, T.D., Ionospheric tomography algorithms, *Imag. Sys. Technol., 5*, 75, 1994

Russell, C. T., and R. C. Elphic, ISEE observations of flux transfer events at the dayside magnetopause, *Geophys. Res. Lett., 6*, 33, 1979.

Russell, C. T., The structure of the magnetopause, in *Physics of the Magnetopause*, *Geophys. Monogr. Ser.*, vol. 90, edited by P. Song, B. U. O. Sonnerup, and M. F. Thomsen, p. 81. AGU, Washington, D. C., 1995.

Scholer, M., Magnetic flux transfer at the magnetopause based on single X line bursty reconnection, *Geophys. Res. Lett., 15*, 291, 1988.

Scholer, M., Models of flux transfer events, in *Physics of the Magnetopause*, *Geophys. Monogr. Ser.*, vol. 90, edited by P. Song, B. U. O. Sonnerup, and M. F. Thomsen, p. 235. AGU, Washington, D. C., 1995.

Sergeev, V. A., V. Angelopoulos, D. G. Mitchell, and C. T. Russell, In situ observations of magnetotail reconnection prior to the onset of a small substorm, *J. Geophys. Res., 100*, 19121, 1995.

Southwood, D. J., C. J. Farrugia, and M. A. Saunders, What are flux transfer events?, *Planet. Space Sci., 36*, 503, 1988.

Wang, X., A. Bhattacharjee, and A. T. Y. Lui, Collisionless tearing instability in magnetotail plasmas, *J. Geophys. Res., 95*, 15047, 1990.

V. Angelopoulos, S. Bale, C. W. Carlson, R. E. Ergun, D. E. Larson, T. Phan, I. Roth, and D. Taylor, Space Sciences Laboratory, University of California, Berkeley, CA 94720. (ree@ssl.berkeley.edu)

J. Raeder, Institute of Geophysics and Planetary Physics, University of California, Los Angeles, CA 90024. (jraeder@igpp.ucla.edu)

T. Bell and U. S. Inan, Stanford Star Laboratory, Stanford University, Stanford, CA 94305. (bell@nova.stanford.edu).

J. -L. Bougeret and R. Manning, CNRS Observatoire de Paris-Meudon, Dept Recherche Spatial, 5 Place Jules Janssen, Meudon, France. (Jean-Louis.Bougeret@obspm.fr)

(Received June 19, 1998; revised March 31, 1999; accepted March 31, 1999.)